

Article

# Numerical Computation of Ag/Al<sub>2</sub>O<sub>3</sub> Nanofluid over a Riga Plate with Heat Sink/Source and Non-Fourier Heat Flux Model

S. Divya<sup>1</sup>, S. Eswaramoorthi<sup>1,\*</sup> and Karuppusamy Loganathan<sup>2,\*</sup><sup>1</sup> Department of Mathematics, Dr. N.G.P. Arts and Science College, Coimbatore 641035, Tamil Nadu, India<sup>2</sup> Department of Mathematics and Statistics, Manipal University Jaipur, Jaipur 303007, Rajasthan, India

\* Correspondence: eswaran.bharathiar@gmail.com (S.E.); loganathankaruppusamy304@gmail.com (K.L.)

**Abstract:** The main goal of the current research is to investigate the numerical computation of Ag/Al<sub>2</sub>O<sub>3</sub> nanofluid over a Riga plate with injection/suction. The energy equation is formulated using the Cattaneo–Christov heat flux, non-linear thermal radiation, and heat sink/source. The leading equations are non-dimensionalized by employing the suitable transformations, and the numerical results are achieved by using the MATLAB bvp4c technique. The fluctuations of fluid flow and heat transfer on porosity, Forchheimer number, radiation, suction/injection, velocity slip, and nanoparticle volume fraction are investigated. Furthermore, the local skin friction coefficient (SFC), and local Nusselt number (LNN) are also addressed. Compared to previously reported studies, our computational results exactly coincided with the outcomes of the previous reports. We noticed that the Forchheimer number, suction/injection, slip, and nanoparticle volume fraction factors slow the velocity profile. We also noted that with improving rates of thermal radiation and convective heating, the heat transfer gradient decreases. The 40% presence of the Hartmann number leads to improved drag force by 14% and heat transfer gradient by 0.5%. The 20% presence of nanoparticle volume fraction leads to a decrement in heat transfer gradient for 21% of Ag nanoparticles and 18% of Al<sub>2</sub>O<sub>3</sub> nanoparticles.

**Keywords:** nanofluid; riga plate; heat source/sink; non-linear thermal radiation; Cattaneo–Christov heat flux



**Citation:** Divya, S.; Eswaramoorthi, S.; Loganathan, K. Numerical Computation of Ag/Al<sub>2</sub>O<sub>3</sub> Nanofluid over a Riga Plate with Heat Sink/Source and Non-Fourier Heat Flux Model. *Math. Comput. Appl.* **2023**, *28*, 20. <https://doi.org/10.3390/mca28010020>

Academic Editors: Mehmet Yavuz and Ioannis Dassios

Received: 21 December 2022

Revised: 29 January 2023

Accepted: 1 February 2023

Published: 3 February 2023



**Copyright:** © 2023 by the authors. Licensee MDPI, Basel, Switzerland. This article is an open access article distributed under the terms and conditions of the Creative Commons Attribution (CC BY) license (<https://creativecommons.org/licenses/by/4.0/>).

## 1. Introduction

The importance of nanofluids has piqued the interest of many industrial researchers. Nanofluid combines base fluids and nanoparticles (1–100 nm). Nanoparticles typically have better thermal distribution properties than convectional heat distribution liquids. Various researchers have been drawn to nanofluid in the last decade, with Choi and Eastman [1] being the first person to come up with the word nanofluid. Martin et al. [2] combined and analyzed a porous medium with nanofluids to increase heat transmission around a vertical finned cylindrical antenna. They detected that the nanoparticle volume fraction is enhanced when mounting the porosity parameter. Uddin et al. [3] examined a single-phase CuO–water nanofluid flow through an isosceles triangular geometry. They observed that the heat transmission is enhanced when the nanoparticle volume fraction increases. The copper-water nanofluid flow over a rotating disk was examined by Nayak et al. [4]. The heat transfer analysis of a nanofluid on a non-linearly stretching plate was scrutinized by Adem and Kishan [5]. The consequences of surface waves on heat transmission and flow were studied by Uddin et al. [6]. They observed that the nanofluids with a lower nanoparticle volume fraction have higher flow configurations. Verma et al. [7] investigated the copper-water nanofluid over a porous medium. They found that the velocity declines when enriching the nanoparticle volume fraction. The MHD flow of a Casson–Williamson nanofluid over a porous medium was examined by Yousef et al. [8]. Mohamed et al. [9] scrutinized the heat transfer flow of Ag–Al<sub>2</sub>O<sub>3</sub>/water-hybrid nanofluid over a stretching sheet. They found that the SFC increased due to a rise in the nanoparticle volume fraction.

Shahzad et al. [10] investigated the heat transfer of copper-nanofluid slip flow over a convective heated sheet. They noted that the SFC decreases when increasing the volume fraction parameter.

The Riga plate plays a vital role in enhancing the electrical conductivity. This plate consists of electrodes and magnets that are arranged alternatively. Gailitis and Lielausis [11] were the first to commence the Riga plate, which generates a Lorentz force parallel to the flow-controlling wall. The mixed convective flow of nanofluid flow on a Riga plate was initiated by Vaidya et al. [12]. They revealed that the warmness of the fluid downturns when improving the modified Hartmann number. Shah et al. [13] inspected the flow of Maxwell fluid through a Riga plate with the generalized Fourier's law. Rizwana and Nadeem [14] analyzed the unsteady MHD flow of copper-water nanofluid past a Riga plate. They found that the MBL thickens when escalating the modified Hartmann number. The Maxwell fluid flow passing through a Riga plate was analyzed by Ramesh et al. [15]. Abbas et al. [16] scrutinized the nanofluid flow over a Riga plate with entropy generation. The hyperbolic nanofluid flow over a Riga plate was numerically studied by Waqas et al. [17]. Eswaramoorthi et al. [18] implemented the double stratification of a Darcy–Forchheimer flow over a Riga plate. They revealed that increasing the modified Hartmann number causes a significant increase in wall shear stress. The microorganisms swimming in the Sutterby nanofluid, passed through a Riga plate, was inspected by Faizan et al. [19]. They proved that the fluid speed is able to enhance the modified Hartmann number. Karthik et al. [20] explored the swimming microorganisms of zero and non-zero mass flux over a Riga plate. They revealed that the fluid speed declines when it strengthens the modified Hartmann number. Parvine and Alam [21] examined the MHD nanofluid flows across a Riga plate. Computational study of a micropolar nanofluid moving in a stratified pattern over a Riga plate was investigated by Rafique et al. [22].

Generally, two types of internal heat generation/consumption occur. The first type of internal heat sink/source depends on the warmth of the fluid. The second type is a non-uniform heat sink/source that depends on warmth and space. Recently, many researchers have been working on heat sinks and sources. An even more intriguing debate on the effects of a non-uniform heat sink/source was dealt with by Madhukesh et al. [23]. It is found that the warmness of the fluid increases when raising the heat sink/source parameter. Oke et al. [24] identified the water nanoparticles of 47-nm alumina over a heat sink/source. They proved that the LNN is proportional when the heat transfer rate amplifies. The heat sink/source of Jeffrey fluid over a heat and mass transfer was scrutinized by Qasim [25]. He identified that when the heat sink parameter is raised, the temperature drops. The effects of Darcy–Forchheimer flow in an unsteady MHD viscous fluid over a non-uniform heat sink/source was investigated by Sharma and Gandhi [26]. Vieru et al. [27] explored the impact of unsteady flow of viscous fluid with a heat sink/source. The non-uniform heat sink/source of Jeffrey and Maxwell nanofluid using a stretching sheet was investigated by Sandeep and Sulochana [28]. They discovered that the thermal boundary layer thickness increases as the values of the non-uniform heat source or sink parameters are increased. Jena et al. [29] inspected the movement of a fluid with a high viscosity past a heat sink/source. The MHD-mixed convective flow of micropolar fluid past an SS with a non-uniform heat sink/source was studied by Sandeep and Sulochana [30]. Reddy and Rao [31] scrutinized the chemical reaction in the heat and mass transfer of nanofluids containing  $\text{Al}_2\text{O}_3$ -water and Ag-water through a vertical cone. They revealed that heat source/sink characteristics lead to improving the temperature profile. A few key researches on this perception have been gathered in Refs. ([32,33]).

Thermally radiative flow is typically encountered when there is a significant warmth difference between the free stream and the surface, and it is important in many industrial processes. Most of the research is based on the Rosseland approximation with linearization, however, this concept is most useful when the warmth difference between ambient and liquid is minuscule, and this difference is typically very significant in many industrial situations. A non-linearized Rosseland approximation is applicable for overcoming this

constraint. Rashidi et al. [34] analyzed the buoyancy effect of MHD nanofluid flow with thermal radiation. They noted that the magnetic and radiation parameters affect the skin friction coefficient. The radiative nanofluid flow over an SS with convective boundary conditions was investigated by Kameswaran et al. [35]. Maleki et al. [36] investigated the radiation impact of a nanofluid flow over a porous plate. They noticed that the local Nusselt number declines when the radiation parameter is increased. The 3D radiative flow of carbon nanotubes in glycerin flown past a Riga plate was addressed by Eswaramoorthi et al. [37]. They proved that increasing the radiation parameter develops the entropy profile. The effect of thermal radiation of a Walters'-B nanofluid was depicted by Mahat et al. [38]. They proved that the temperature of the fluid upgrades to strengthen the thermal radiation. Mahanthesh et al. [39] examined the boundary layer flow of a melting plate with non-linear thermal radiation. The Darcy–Forchheimer flow of an Eyring–Powell nanofluid with non-linear thermal radiation was explored by Bhatti et al. [40]. The thermally radiative flow of Casson–Williamson nanofluid with binary chemical reaction was investigated by Eswaramoorthi et al. [41]. They noticed that when the radiation parameter is increased, the heat transfer gradient rises. Mahanta et al. [42] analyzed the 3D MHD nanofluid flow passing through an SS with non-linear radiation. They identified that the higher thermal radiation parameter leads to develop the Bejan number. The influence of radiation on a magnetohydrodynamic (MHD) three-dimensional stagnation-point flow of a graphene oxide nanofluid based on water and produced by a non-uniform heat source/sink over a horizontal plane surface was investigated by Waqas et al. [43]. They noticed that the temperature profile increased as the radiation parameter increased. A few cutting-edge research reports have been gathered in Refs. ([44–46]).

According to study findings in the literature, as mentioned above, the majority of the researchers are working to discover the nature of the radiative flow of nanofluid with non-uniform heat sink/source and Cattaneo–Christov heat flux past an SS but have yet to be analyzed through a Riga plate with velocity slip. As a result, our primary objective is to fill this knowledge gap. Our research describes the consequence of non-linear thermal radiation, non-uniform heat sink/source, and Cattaneo–Christov of Darcy–Forchheimer flow of water-based (Ag and Al<sub>2</sub>O<sub>3</sub>) nanoparticles past a Riga plate with a slip condition, because the upshot of slip is more crucial when the particles' mean free path is tantamount or smaller than the problem's usual structure. In these situations, the continuance flow presumptions are limited. In such places, the slip boundary presumptions act a vital role in restraining the flow attributes (e.g., see Aldabesh et al. [47]). The primary goal of utilizing nanoparticles, such as Ag and Al<sub>2</sub>O<sub>3</sub>, is as nanofluid coolant for contemporary engines. This work will be useful for thermal engineers in developing models of thermal systems. The key takeaways of this study can be summed up as follows:

1. Modify the current mathematical model to include nanofluids based on Ag/Al<sub>2</sub>O<sub>3</sub>-water, Cattaneo–Christov heat flux, non-linear thermal radiation, and heat source/sink.
2. In what ways does it affect Darcy–Forchheimer flow on a Riga plate?
3. Exactly how do the Cattaneo–Christov heat flux phenomenon and non-linear thermal radiation influence heat transfer?
4. When convective heating conditions are applied, how does the heat transfer gradient respond?

## 2. Mathematical Formulation

We explored the 2D Darcy–Forchheimer flow of water-based Ag/Al<sub>2</sub>O<sub>3</sub> nanoparticles past a heated Riga plate. We consider that the  $x$ -axis should be aligned in the same direction as the plate, but the  $y$ -axis should be perpendicular to it. The heat equation is constructed by non-linear thermal radiation, Cattaneo–Christov theory and a non-uniform heat sink/source. Let  $T_w$  and  $T_\infty (\leq T_w)$  be the fluid temperature and free stream temperature, respectively. The bottom of the plate was heated by passing hot fluid with temperature  $T_f$  and this generate a heat transfer coefficient  $h_c$ . The sketch of the Riga plate and the flow

model are shown in Figure 1a,b. The equations of mass, momentum, and energy with their associated constraints are shown below (e.g., Kameswaran et al. [35], Maleki et al. [36]).

$$\frac{\partial u}{\partial x} + \frac{\partial v}{\partial y} = 0, \tag{1}$$

$$u \frac{\partial u}{\partial x} + v \frac{\partial u}{\partial y} = \nu_{nf} \frac{\partial^2 u}{\partial y^2} - \frac{\nu_{nf}}{k_1^*} u - \frac{c_b}{\sqrt{k^*}} u^2 + \frac{\pi J_0 M}{8 \rho_{nf}} \text{Exp} \left[ -\frac{\pi}{a_1} y \right], \tag{2}$$

$$\begin{aligned} u \frac{\partial T}{\partial x} + v \frac{\partial T}{\partial y} &= \frac{k_{nf}}{(\rho c_p)_{nf}} \frac{\partial^2 T}{\partial y^2} + \frac{16 \sigma^*}{3 k^* (\rho C_p)_{nf}} \frac{\partial}{\partial y} \left( T^3 \frac{\partial T}{\partial y} \right) - \lambda \left[ u^2 \frac{\partial^2 T}{\partial x^2} \right. \\ &+ v^2 \frac{\partial^2 T}{\partial y^2} + 2uv \frac{\partial^2 T}{\partial x \partial y} + \left( u \frac{\partial u}{\partial x} + v \frac{\partial u}{\partial y} \right) \frac{\partial T}{\partial x} + \left( u \frac{\partial v}{\partial x} + v \frac{\partial v}{\partial y} \right) \frac{\partial T}{\partial y} \left. \right] \\ &+ \frac{1}{(\rho c_p)_{nf}} \frac{k_{nf} U_w}{x \nu_{nf}} [A^* (T_f - T_\infty) f' + B^* (T - T_\infty)]. \end{aligned} \tag{3}$$

The corresponding boundary conditions, see Mahmood et al. [48] and Hayat et al. [49]:

$$\begin{aligned} u = U_w + \mu_{nf} \frac{\partial u}{\partial y}, \quad v = -V_w, \quad -k_{nf} T_y = h_c [T_f - T] \quad \text{at } y = 0 \\ u \rightarrow 0, v \rightarrow 0, T \rightarrow T_\infty \quad \text{as } y \rightarrow \infty \end{aligned} \tag{4}$$

In order to solve the governing system of PDEs (1)–(4), stream function  $\psi$  is introduced, as seen in Afify [50].

$$\psi = (av_f)^{\frac{1}{2}} x f(\zeta), \quad u = \frac{\partial \psi}{\partial y}, \quad v = -\frac{\partial \psi}{\partial x}. \tag{5}$$

Define the variables,

$$\zeta = \sqrt{\frac{a}{\nu_f}} y, \quad u = ax f'(\zeta), \quad v = -\sqrt{av_f} f(\zeta), \quad \theta = \frac{T - T_\infty}{T_f - T_\infty}. \tag{6}$$

Considering the aforementioned changes, Equations (2) and (3) are written as follows:

$$\frac{1}{A_1 A_2} f'''(\zeta) + f(\zeta) f''(\zeta) - f'^2(\zeta) - \frac{1}{A_1 A_2} \lambda f'(\zeta) - Fr f'^2(\zeta) + \frac{1}{A_2} Ha \text{Exp}[-\beta_R \zeta] = 0, \tag{7}$$

$$\begin{aligned} f(\zeta) \theta'(\zeta) + \left[ \frac{A_5}{A_3} \frac{1}{Pr} \right] \theta''(\zeta) + \frac{A_1 A_2 A_5}{A_3} \frac{1}{Pr} [A^* f'(\zeta) + B^* \theta(\zeta)] - \Gamma_1 \{ f^2(\zeta) \theta''(\zeta) \\ + f(\zeta) f'(\zeta) \theta'(\zeta) \} + \frac{1}{Pr} \frac{1}{A_3} \frac{4}{3} Rd \left[ (\theta_w - 1)^3 \{ 3\theta^2(\zeta) \theta'^2(\zeta) + \theta^3(\zeta) \theta''(\zeta) \} + (\theta_w - 1)^2 \right. \\ \left. \{ 6\theta(\zeta) \theta'^2(\zeta) + 3\theta^2(\zeta) \theta''(\zeta) \} + (\theta_w - 1) \{ 3\theta'^2(\zeta) + 3\theta(\zeta) \theta''(\zeta) \} + \theta''(\zeta) \right] = 0. \end{aligned} \tag{8}$$

The appropriate boundary conditions (4) are remodeled as follows,

$$\begin{aligned} f(0) = fw, \quad f'(0) = 1 + \frac{\Lambda}{A_1} f''(0), \quad f'(\infty) = 0, \\ \theta'(0) = -\frac{Bi}{A_5} [1 - \theta(0)], \quad \theta(\infty) = 0. \end{aligned} \tag{9}$$

The skin friction coefficient and local Nusselt number can be expressed as follows,

$$C_f \sqrt{Re} = \frac{1}{A_1} f''(0),$$

$$\frac{Nu}{\sqrt{Re}} = - \left[ A_5 + \frac{4}{3} Rd \{ 1 + \theta(0)(\theta_w - 1) \}^3 \right] \theta'(0)$$

The nomenclature section specifies all the variables involved in the flow.

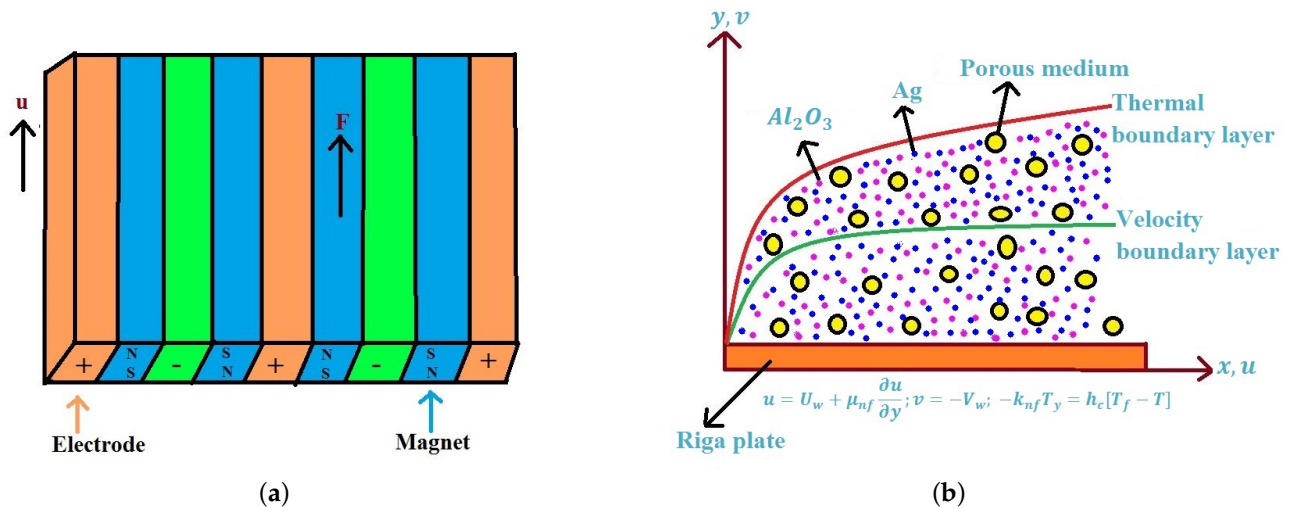


Figure 1. (a) Sketch of a Riga plate and (b) physical configuration of the flow model.

### 3. Numerical Solution

The MATLAB bvp4c technique is used to solve the remodeled ODEs (Equations (7) and (8)) and corresponding boundary conditions (9). In this case, the coupled non-linear PDEs and the boundary conditions can be transformed into five equivalent first-order ODEs and boundary conditions, respectively, see Asshaari et al. [51] and Shampine et al. [52]. To carry out this procedure, we must do the following:

$$f = K_1, f' = K_2, f'' = K_3, \theta = K_4, \theta' = K_5$$

The system of equations are

$$K'_1 = K_2$$

$$K'_2 = K_3$$

$$K'_3 = A_1 A_2 \left[ K_2^2 - K_1 K_3 + \frac{1}{A_1 A_2} \lambda K_2 + Fr K_2^2 - \frac{1}{A_2} Ha Exp[-\beta_R \zeta] \right]$$

$$K'_4 = K_5$$

$$K'_5 = \frac{B_1}{B_2}$$

where

$$B_1 = -K_1 K_5 - \frac{A_1 A_2 A_5}{A_3} \frac{1}{Pr} [A^* K_2 + B^* K_4] + \Gamma_1 \{ K_1 K_2 K_5 \}$$

$$- \frac{1}{Pr} \frac{1}{A_3} \frac{4}{3} Rd \left[ (\theta_w - 1)^3 \{ 3K_4^2 K_5^2 \} + (\theta_w - 1)^2 \{ 6K_4 K_5^2 \} + (\theta_w - 1) \{ 3K_5^2 \} \right]$$

$$B_2 = \frac{A_5}{A_3 Pr} - \Gamma_1 (K_2^2) + \frac{1}{Pr} \frac{1}{A_3} \frac{4}{3} Rd \left[ (\theta_w - 1)^3 \{ K_4^3 \} + (\theta_w - 1)^2 \{ 3K_4^2 \} + (\theta_w - 1) \{ 3K_4 \} + 1 \right]$$

With the corresponding conditions

$$K_1(0) = fw, K_2(0) = 1 + \frac{\Lambda}{A_1}K_3(0), K_2(\infty) = 0,$$

$$K_5(0) = -\frac{Bi}{A_5}[1 - K_4(0)], K_4(\infty) = 0$$

The advantage of this method is the ability to handle non-linear problems in simple domains more quickly. The technique is shown to be efficient and accurate in various boundary value scenarios, all described in Shampine et al. [53]. The process repeats itself further until a tolerance of  $10^{-5}$  and a step size of 0.05 is reached.

#### 4. Results and Discussion

The primary goal of this segment is to provide a clear understanding of the flow regime, specifically, the variations in the nanofluid velocity, nanofluid temperature, skin friction coefficient, and local Nusselt number for both nanoparticles (Ag and Al<sub>2</sub>O<sub>3</sub>) as a result of various regulatory flow parameters. Table 1 provides the physical properties of nanoparticles (Ag and Al<sub>2</sub>O<sub>3</sub>) and base fluid (H<sub>2</sub>O). The nanofluid specifications are depicted in Table 2. Table 3 provides a comparison of  $-f''(0)$  to Prabakaran et al. [54], Ibrahim and Shankar [55] for different values of  $fw$  with  $\lambda = Fr = Ha = \phi = 0$  and observed that our numerical results corresponded perfectly with theirs. The fluctuations of Ag nanoparticle on SFC and LNN for different values of  $\lambda, Fr, Ha, fw, \Lambda$ , and  $\phi$  are portrayed in Table 4. Table 5 represents the fluctuations of Al<sub>2</sub>O<sub>3</sub> nanoparticles on SFC and LNN for different values of  $\lambda, Fr, Ha, fw, \Lambda$ , and  $\phi$ . From Tables 4 and 5 it is detected that the surface drag force ( $C_f Re^{1/2}$ ) decimates when augmenting the values of  $\lambda, Fr, fw$ , and  $\phi$  and it augments for the larger quantities of  $Ha$ , and  $\Lambda$ . The heat transfer rate of ( $Nu Re^{-1/2}$ ) decreases when increasing the size of  $\lambda, Fr, \Lambda$  and  $\phi$  and is enhanced for larger values of the modified Hartmann number and injection/suction parameter. Table 6 shows the consequence of  $A^*, B^*, \Gamma_1, Rd$  and  $Bi$  on LNN. It is observed that the LNN slumps when enhancing the values of  $A^*$  and  $B^*$  and it improves when increasing the quantity of  $\Gamma_1, Rd$  and  $Bi$ .

**Table 1.** The thermo-physical properties of the nanomaterials and water, see Roja and Giresha [56].

Physical Properties	Silver (Ag)	Aluminium Oxide (Al <sub>2</sub> O <sub>3</sub> )	Water (H <sub>2</sub> O)
$\rho / (\text{kg}/\text{m}^{-3})$	10,500	3970	997.1
$C_p / (\text{J} \cdot \text{kg}^{-1} \cdot \text{K}^{-1})$	235	765	4179
$\sigma / (\Omega \cdot \text{m})^{-1}$	$6.3 \times 10^7$	$3.5 \times 10^7$	$5.5 \times 10^{-6}$
$k / (\text{W} \cdot \text{m}^{-1} \cdot \text{K}^{-1})$	429	40	0.613

**Table 2.** Physical characteristics, see Sharma [26].

Properties	Nanofluid
Viscosity ( $\mu$ )	$A_1 = \frac{\mu_f}{\mu_{nf}} = (1 - \phi)^{2.5}$
Density ( $\rho$ )	$A_2 = \frac{\rho_{nf}}{\rho_f} = \left(1 - \phi + \phi \frac{\rho_s}{\rho_f}\right)$
Heat capacity ( $\rho C_p$ )	$A_3 = \frac{(\rho C_p)_{nf}}{(\rho C_p)_f} = \left(1 - \phi + \phi \frac{(\rho C_p)_s}{(\rho C_p)_f}\right)$
Electrical conductivity ( $\sigma$ )	$A_4 = \frac{\sigma_{nf}}{\sigma_f} = 1 + \frac{3\left(\frac{\sigma_s}{\sigma_f} - 1\right)\phi}{\left(\frac{\sigma_s}{\sigma_f} + 2\right) - \left(\frac{\sigma_s}{\sigma_f} - 1\right)\phi}$
Thermal conductivity ( $k$ )	$A_5 = \frac{k_{nf}}{k_f} = \frac{k_s + (m-1)k_f - (m-1)\phi(k_f - k_s)}{k_s + (m-1)k_f + \phi(k_f - k_s)}$

**Table 3.** Comparison of  $-f''(0)$  for disparate values of  $fw$  with  $\lambda = Fr = Ha = \phi = 0$  to Prabakaran et al. [54], Ibrahim and Shankar [55].

$fw$	Present Study	Ref. [54]	Ref. [55]
0	1.000001	1.000000	1.0000
0.5	1.280776	1.280776	1.2808

**Table 4.** SFC & LNN comparison for diverse combo of  $\lambda, Fr, Ha, fw, \Lambda, \phi$ .

$\lambda$	$Fr$	$Ha$	$fw$	$\Lambda$	$\phi$	Ag		
						$C_f$	$Nu$	
0.2	0.4	0.3	0.5	1	0.05	-0.540406	0.722099	
						-0.549413	0.721707	
						-0.557932	0.721327	
						-0.566000	0.720961	
						-0.573647	0.720606	
0.2	0.4	0.3	0.5	1	0.05	-0.540406	0.722099	
						-0.553538	0.721507	
						-0.565041	0.720977	
						-0.575249	0.720498	
						-0.584406	0.720062	
0.2	0.4	0	0.5	1	0.05	-0.598291	0.719486	
						-0.578264	0.720432	
						-0.559002	0.721299	
						-0.540406	0.722099	
						-0.522401	0.722842	
0.2	0.4	0.3	-0.6	1	0.05	-0.409777	0.139884	
						-0.453539	0.455283	
						-0.477364	0.571358	
						-0.502169	0.649742	
						-0.553210	0.738959	
0.2	0.4	0.3	0.5	0.2	0.05	-1.198806	0.730271	
						-0.911637	0.727170	
						-0.739594	0.725004	
						-0.623925	0.723378	
						-0.540406	0.722099	
0.2	0.4	0.3	0.5	1	0	-0.474647	0.772332	
						0.05	-0.540406	0.722099
						0.1	-0.590914	0.680030
						0.15	-0.632065	0.644168
						0.2	-0.666931	0.613247

Figure 2a–d portray the outcomes of  $\lambda, Fr, Ha$  and  $fw$  on the nanofluid velocity profile. The results show that a larger modified Hartmann number values increases the nanofluid flow speed, whereas a larger  $\lambda, Fr$ , and  $fw$  result in an opposite behavior. Physically, larger values of the modified Hartmann number produce larger electrical fields, which in turn produce larger values of the wall-parallel Lorentz force experienced by the body. Since this is the case, the fluid’s speed increases. Further, the higher porosity enriches the fluid resistance during flow, which slows down fluid motion and makes the boundary layer thinner. The variations in the slip parameter and nanoparticle volume fraction on the nanofluid velocity profile are illustrated in Figure 3a,b. It is found that the increased availability of  $\Lambda$  and  $\phi$  leads to a decay in the nanofluid velocity. Physically, the fluid deforms as the velocity slip parameter increases because of the low adhesive forces.

**Table 5.** SFC & LNN comparison for a diverse combination of  $\lambda, Fr, Ha, fw, \Lambda, \phi$ .

$\lambda$	$Fr$	$Ha$	$fw$	$\Lambda$	$\phi$	$Al_2O_3$	
						$C_f$	$Nu$
0.2	0.4	0.3	0.5	1	0.05	−0.507314	0.728057
0.3						−0.518302	0.727571
0.4						−0.528618	0.727103
0.5						−0.538316	0.726652
0.6						−0.547446	0.726219
0.2	0.4	0.3	0.5	1	0.05	−0.507314	0.728057
0.8						−0.521096	0.727438
1.2						−0.533185	0.726883
1.6						−0.543925	0.726380
2						−0.553570	0.725921
0.2	0.4	0	0.5	1	0.05	−0.569436	0.725170
0.1		−0.548014				0.726214	
0.2		−0.527336				0.727172	
0.3		−0.507314				0.728057	
0.4		−0.487879				0.728880	
0.2	0.4	0.3	−0.6	1	0.05	−0.393978	0.175973
−0.2			−0.432415			0.479912	
0			−0.453043			0.587601	
0.2			−0.474401			0.660208	
0.6			−0.518389			0.744083	
0.2	0.4	0.3	0.5	0.2	0.05	−1.074296	0.736057
0.4				−0.833493		0.733090	
0.6				−0.684442		0.730967	
0.8				−0.582187		0.729347	
1				−0.507314		0.728057	
0.2	0.4	0.3	0.5	1	0	−0.474647	0.772332
0.05					−0.507314	0.728057	
0.1					−0.538018	0.690530	
0.15					−0.567324	0.658335	
0.2					−0.595710	0.630453	

Figure 4a–d depict the transitions on the temperature distribution for various values of  $A^*, B^*, Rd$  and  $\phi$ . It is demonstrated that the thickness of the TBL increased due to the increased presence of  $A^*, B^*, Rd$ , and  $\phi$ . Physically, strengthening the thermal radiation causes increased energy transport between the particles and this causes an enrichment of the thermal boundary-layer thickness. Figure 5a–d delineates the changes in the temperature profile for disparate values of  $fw, \Gamma_1$  and  $Bi$ . It is revealed that the fluid warmth declines when the values for convective cooling, injection/suction, and the thermal relaxation time parameter are enhanced, and it intensifies for larger values for the convective heating parameter. Physically, improving the convective heating parameter leads to a greater heat transfer coefficient, and this coefficient increases the fluid temperatures and thickens the thermal boundary layer. Also, Ag nanoparticles have a thicker thermal boundary layer compared to the  $Al_2O_3$  nanoparticles. Generally, Ag nanoparticles have higher thermal conductivity than the  $Al_2O_3$  nanoparticles. Figures 6a–d and 7a–d indicate the upshot of  $Fr, Ha, fw, \lambda$  and  $\Lambda$  on the SFC. It is observed that the surface drag force decreases when increasing the  $Fr, \lambda$  and  $fw$  values and it enlarges when heightening the values of  $Ha$  and  $\Lambda$ . The changes of LNN for various combinations of  $Ha, Rd, \Gamma_1, fw$  and  $\lambda$  are illustrated in Figure 8a–d. Based on these graphs, it can be seen that the LNN enlarges when enhancing the values of  $Ha, fw$  and  $\Gamma_1$ , and opposite reaction is observed for larger values of  $\lambda$ . Figure 9a,b shows the consequence of  $A^*, B^*$  and  $fw$  on LNN. It is explored that the LNN decays when enhancing the overall quantity of  $A^*$  and  $B^*$  and it enriches for larger values of  $fw$ .

**Table 6.** Variations of LNN for a diverse combination of  $A^*$ ,  $B^*$ ,  $\Gamma_1$ ,  $Rd$ ,  $Bi$ .

$A^*$	$B^*$	$\Gamma_1$	$Rd$	$Bi$	$Ag$	$Al_2O_3$
0	0.1	0.1	0.6	0.5	0.730125	0.734846
0.2					0.714032	0.721239
0.4					0.697778	0.707516
0.6					0.681362	0.693676
0.8					0.664781	0.679719
0.1	0	0.1	0.6	0.5	0.723775	0.729211
	0.2				0.720341	0.726864
	0.4				0.716550	0.724352
	0.6				0.712333	0.721652
	0.8				0.707854	0.718741
0.1	0.1	0	0.6	0.5	0.712420	0.718396
		0.1			0.722099	0.728057
		0.2			0.731930	0.737842
		0.3			0.741850	0.747699
		0.4			0.759113	0.757502
0.1	0.1	0.1	0	0.5	0.440869	0.442943
			1		0.898688	0.907764
			2		1.305605	1.323422
			3		1.675997	1.701921
			4		2.025144	2.057481
0.1	0.1	0.1	0.6	0.1	0.162427	0.163222
				0.3	0.459119	0.462158
				0.5	0.722099	0.728057
				0.7	0.955640	0.964981
				1	1.259007	1.273932

Figure 10a–d shows the slumping/growing percentage of the SFC for distinct quantities of  $\lambda$ ,  $Fr$ ,  $Ha$  and  $fw$ . In the case of the porosity parameter, the greatest diminishing percentage (2.30%) is collected in viscous fluid when  $\lambda$  is changed from 0.2 to 0.3 and the least diminishing percentage (1.35%) is obtained in Ag nanofluid when  $\lambda$  is changed from 0.5 to 0.6. In the case of  $Fr$ , the greatest diminishing percentage (3.05%) is observed in viscous fluid when  $Fr$  changed from 0.4 to 0.8, and the least diminishing percentage (1.59%) is observed in Ag nanofluid when  $Fr$  is changed from 1.6 to 2. In the case of the modified Hartmann number, the greatest improving percentage (4.33%) is collected in viscous fluid when  $Ha$  is changed from 0.3 to 0.4, and the least improving percentage (3.32%) is obtained in Ag nanofluid when  $Ha$  is changed from 0.2 to 0.3. In the case of the injection/suction parameter, the greatest diminishing percentage (2.59%) is collected in Ag nanofluid when  $fw$  is changed from  $-0.2$  to  $-0.1$  and the least diminishing percentage (2.35%) is obtained in  $Al_2O_3$  nanofluid when  $fw$  is changed from  $-0.5$  to  $-0.4$ . Figure 11a,b shows the declining SFC percentages for a distinct quantity of  $\Lambda$  and  $fw$ . In the case of the slip parameter, the greatest improving percentage (23.95%) is collected in Ag nanofluid when  $\Lambda$  is changed from 0.2 to 0.4, and the least improving percentage (12.35%) is obtained in viscous fluid when  $\Lambda$  is changed from 0.8 to 1. In the case of the injection/suction parameter, the greatest diminishing percentage (2.57%) is collected in Ag nanofluid when  $fw$  is changed from 0 to 0.1, and the least diminishing percentage (2.26%) is obtained in  $Al_2O_3$  nanofluid when  $fw$  is changed from 0.3 to 0.4.

The improving/declining percentages of LNN on  $\lambda$ ,  $Fr$ ,  $Ha$ ,  $Rd$ ,  $A^*$ ,  $B^*$ ,  $Bi$  and  $\Lambda$  are illustrated in Figures 12a–d and 13a–d. In the case of the porosity parameter, the greatest diminishing percentage (0.066%) is collected in  $Al_2O_3$  nanofluid when  $\lambda$  is changed from 0.2 to 0.3, and the least diminishing percentage (0.049%) is obtained in Ag nanofluid when  $\lambda$  is changed from 0.5 to 0.6. In the case of  $Fr$ , the greatest diminishing percentage (0.088%) is collected in viscous fluid when  $Fr$  is changed from 0.4 to 0.8 and the least diminishing percentage (0.060%) is observed in Ag nanofluid when  $Fr$  is changed from 1.6 to 2. In the case of the modified Hartmann number, the greatest improving percentage (0.151%)

is collected in viscous fluid when  $Ha$  is changed from 0 to 0.1, and the least improving percentage (0.102%) is observed in Ag nanofluid when  $Ha$  is changed from 0.3 to 0.4. In the case of non-linear radiation, the greatest improving percentage (119.56%) is collected in viscous fluid when  $Rd$  is changed from 0 to 1, and the least improving percentage (20.76%) is observed in viscous fluid when  $Rd$  is changed from 3 to 4. In the case of  $A^*$ , the greatest diminishing percentage (2.433%) is collected in Ag nanofluid when  $A^*$  is changed from 0.6 to 0.8, and the least diminishing percentage (1.619%) is observed in viscous fluid when  $A^*$  is changed from 0 to 0.2. In the case of  $B^*$ , the greatest diminishing percentage (0.628%) is collected in Ag nanofluid when  $B^*$  is changed from 0.6 to 0.8, and the least diminishing percentage (0.245%) is observed in viscous fluid when  $B^*$  is changed from 0 to 0.2. In the case of the Brinkmann number, the greatest improving percentage (183.14%) is collected in  $Al_2O_3$  nanofluid when  $Bi$  is changed from 0.1 to 0.3, and the least improving percentage (31.74%) is observed in Ag nanofluid when  $Bi$  is changed from 0.7 to 1. In the case of the slip parameter, the greatest diminishing percentage (0.424%) is collected in Ag nanofluid when  $\Lambda$  is changed from 0.2 to 0.4, and the least diminishing percentage (0.173%) is observed in viscous fluid when  $\Lambda$  is changed from 0.8 to 1.

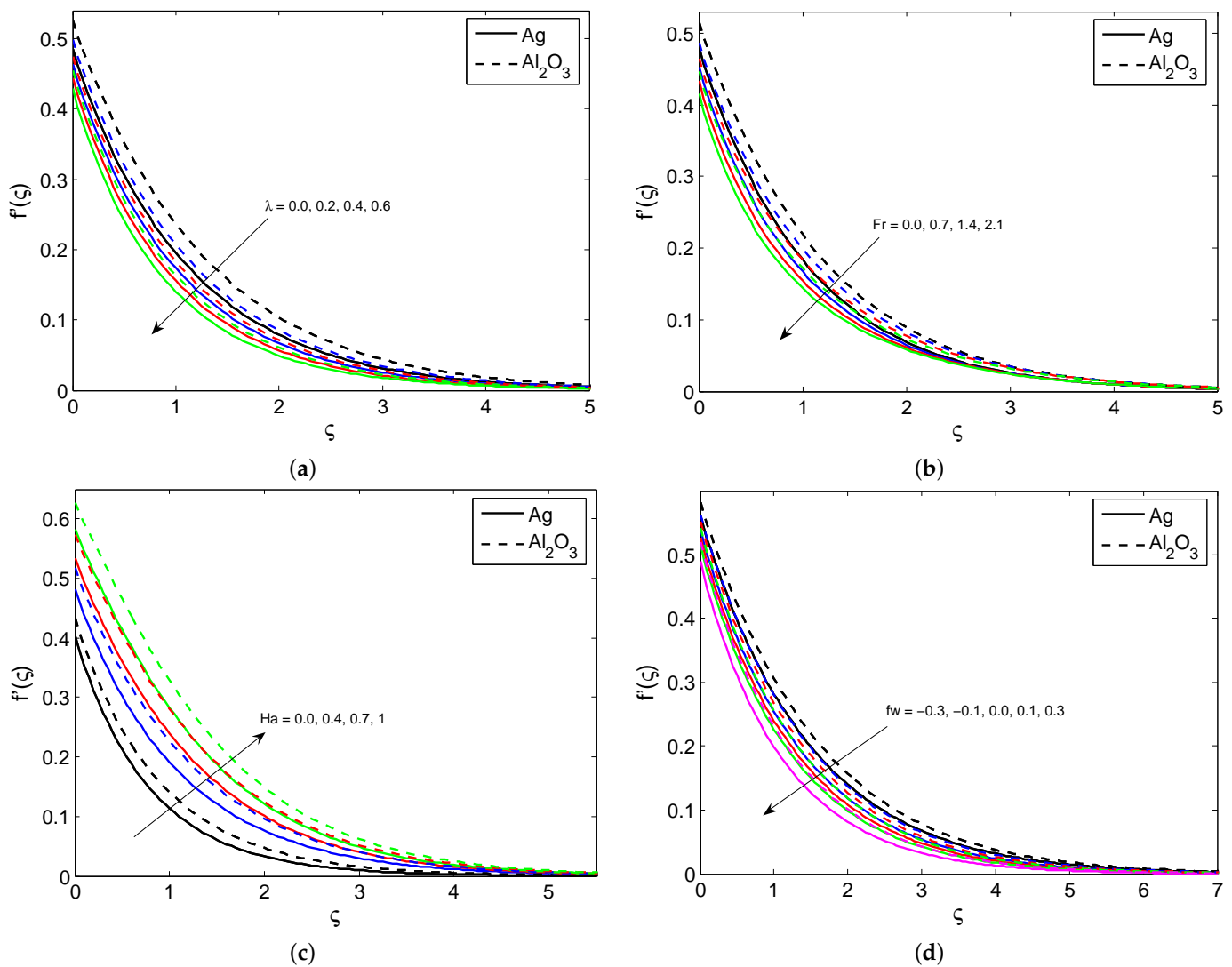


Figure 2. The variation of  $f'(\zeta)$  in relation to (a)  $\lambda$ , (b)  $Fr$ , (c)  $Ha$  and (d)  $fw$ .

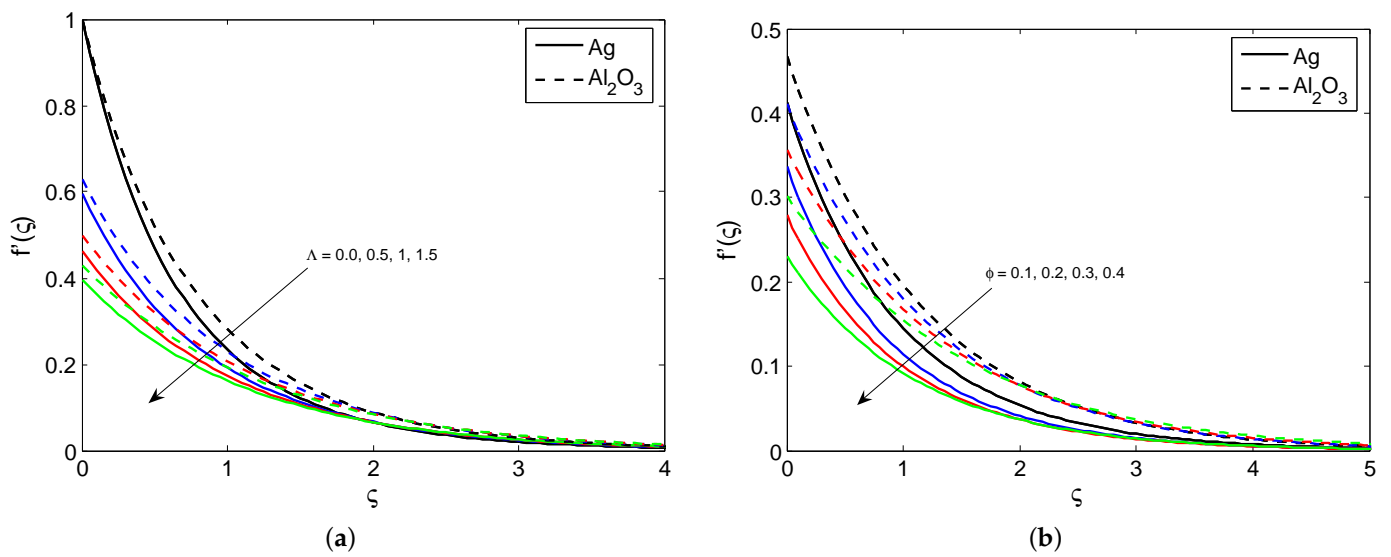


Figure 3. The variation of  $f'(\zeta)$  in relation to (a)  $\Lambda$  and (b)  $\phi$ .

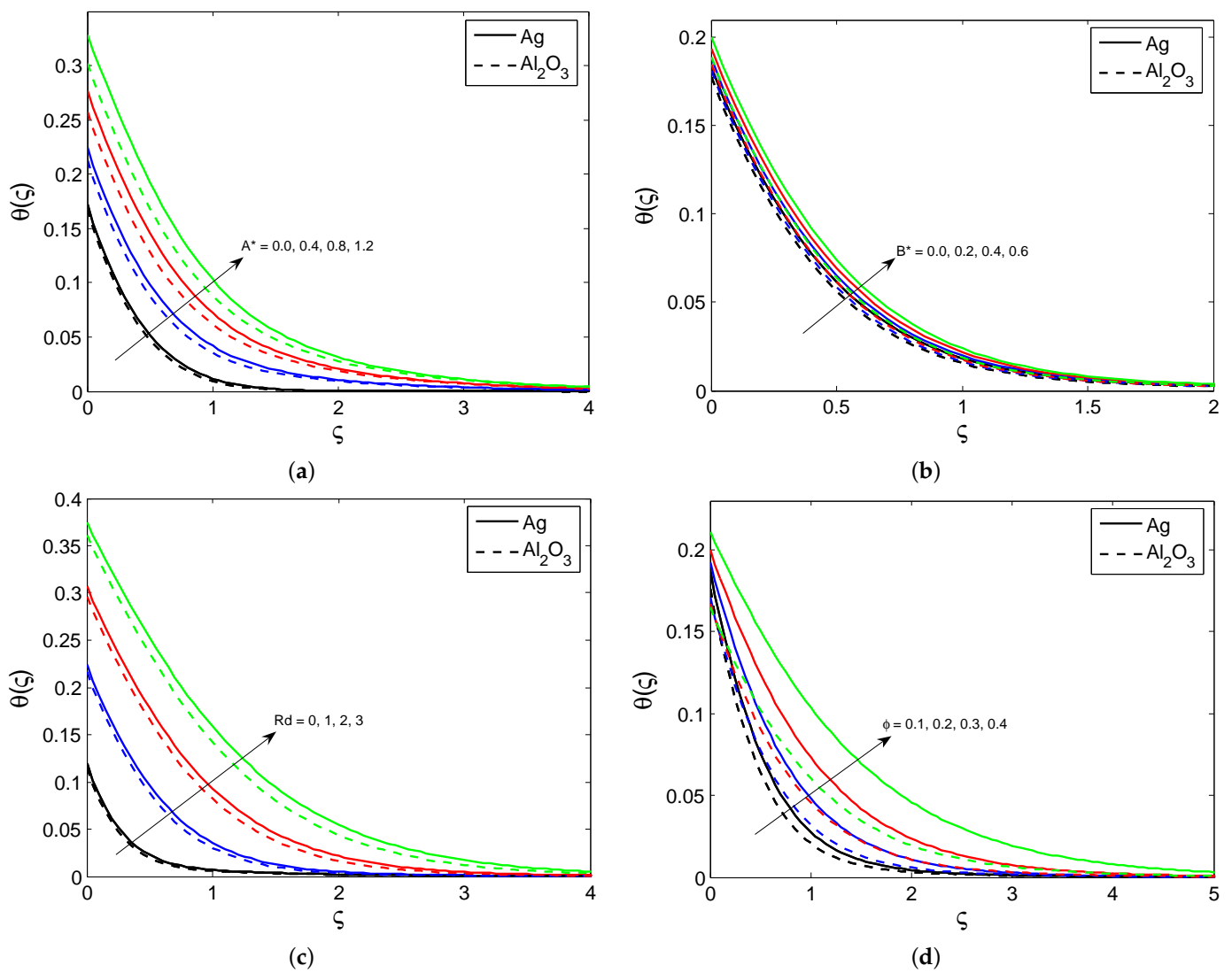
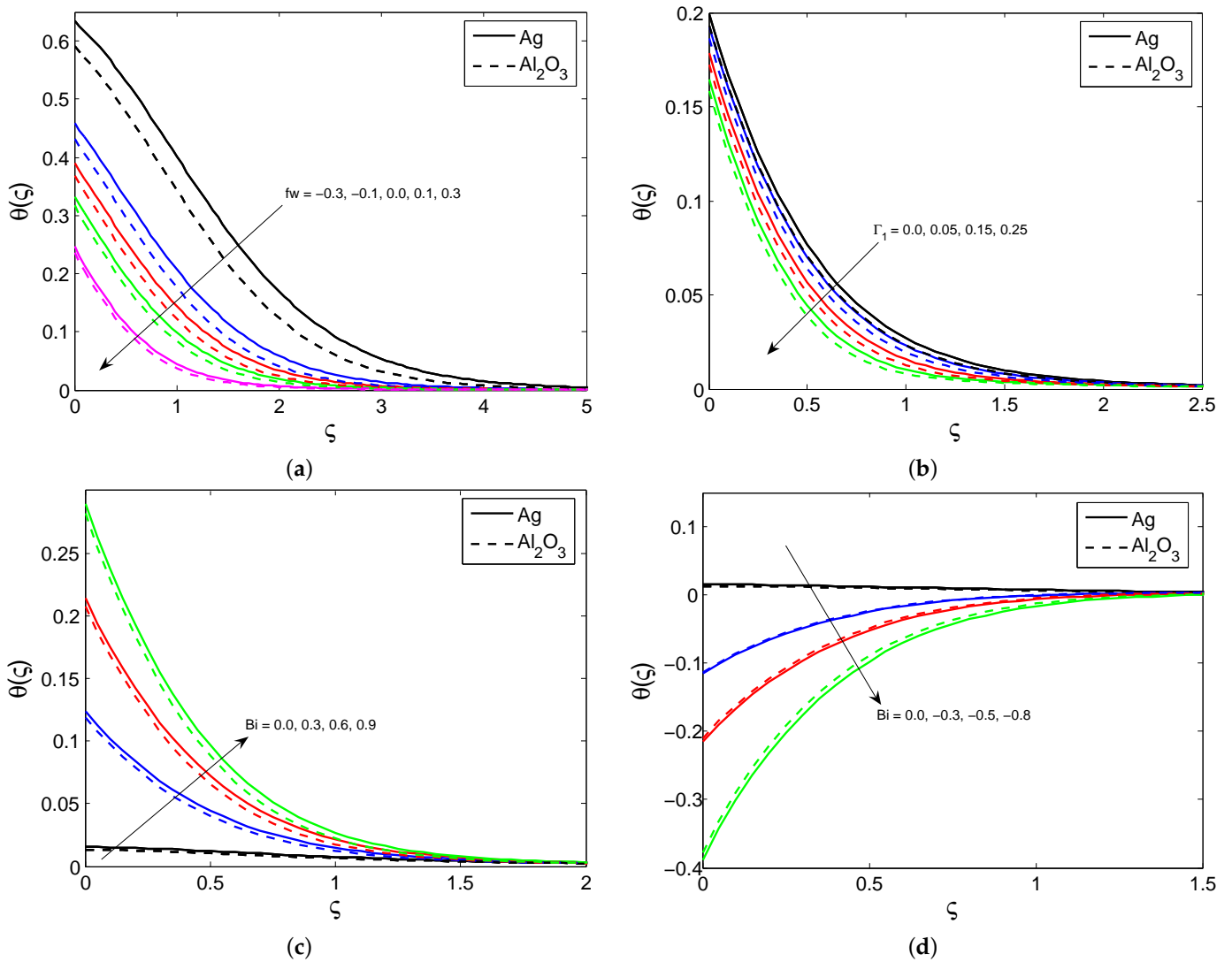
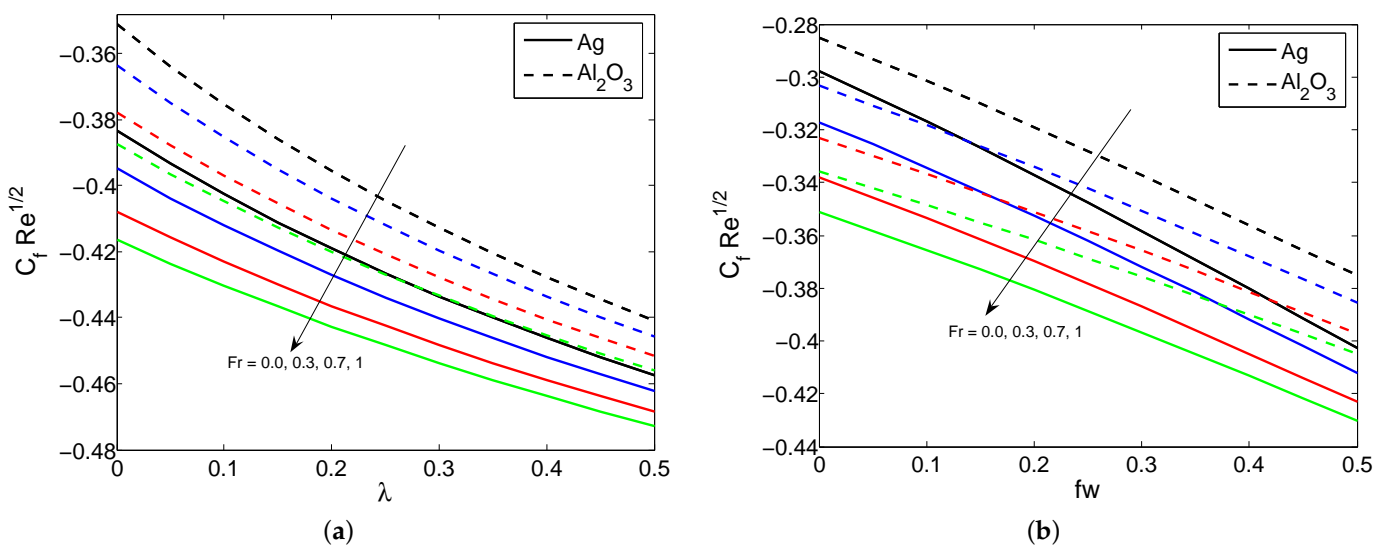


Figure 4. The variation of  $\theta(\zeta)$  in relation to (a)  $A^*$ , (b)  $B^*$ , (c)  $Rd$  and (d)  $\phi$ .



**Figure 5.** The variation of  $\theta(\zeta)$  in relation to (a)  $fw$ , (b)  $\Gamma_1$ , (c)  $Bi$  (convective heating) and (d)  $Bi$  (convective cooling).



**Figure 6.** Cont.

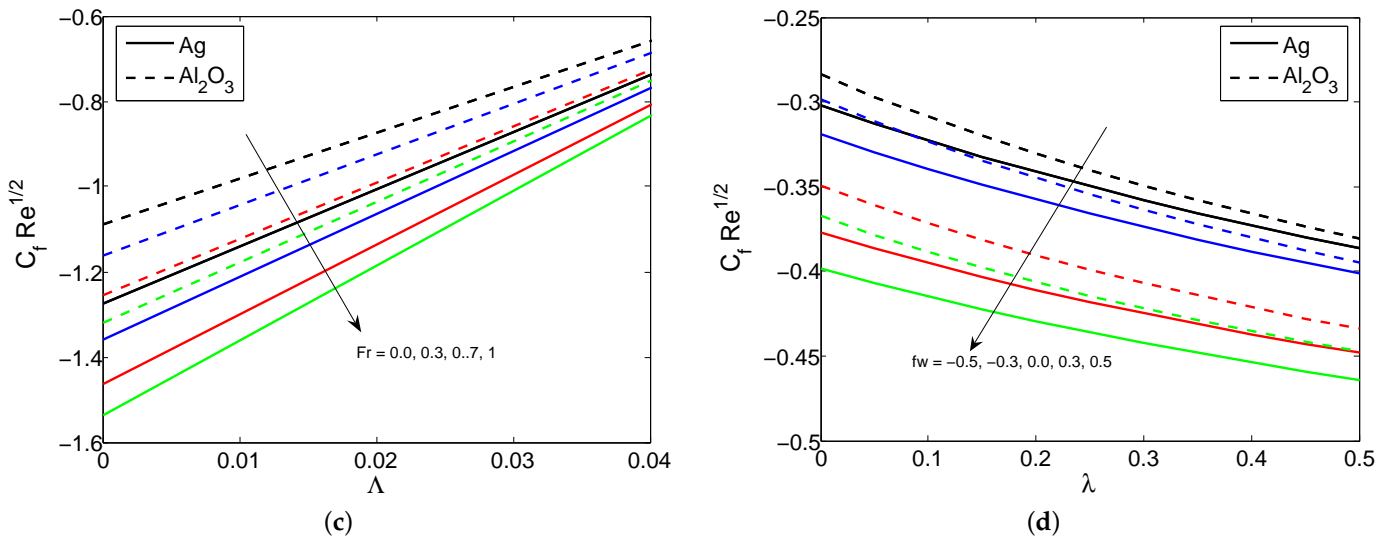


Figure 6. SFC variation for diverging values of (a)  $Fr$  &  $\lambda$ , (b)  $Fr$  &  $fw$ , (c)  $Fr$  &  $\Lambda$  and (d)  $fw$  &  $\Lambda$ .

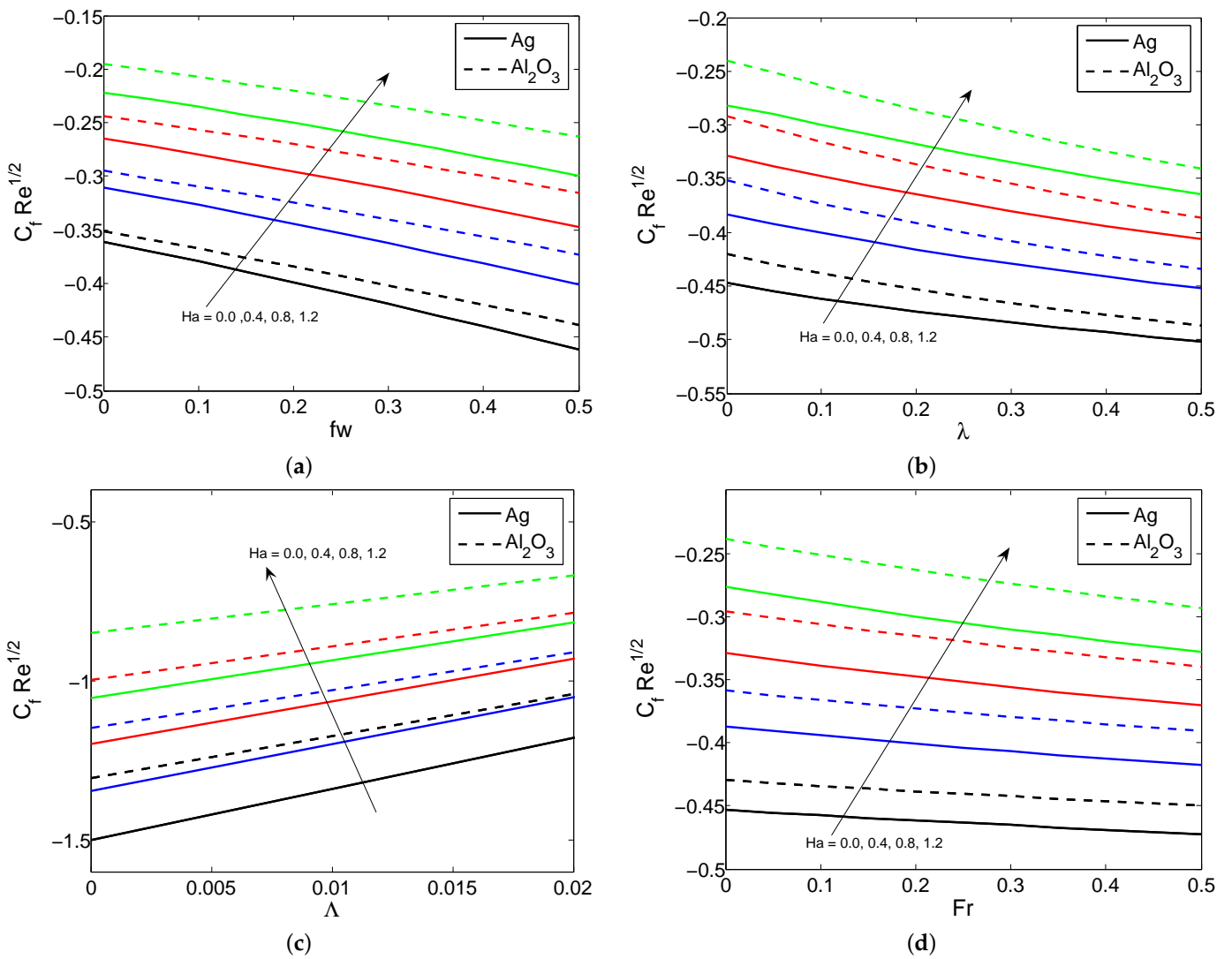


Figure 7. SFC variation for diverging values of (a)  $fw$ , (b)  $\lambda$ , (c)  $\Lambda$  and (d)  $Fr$ .

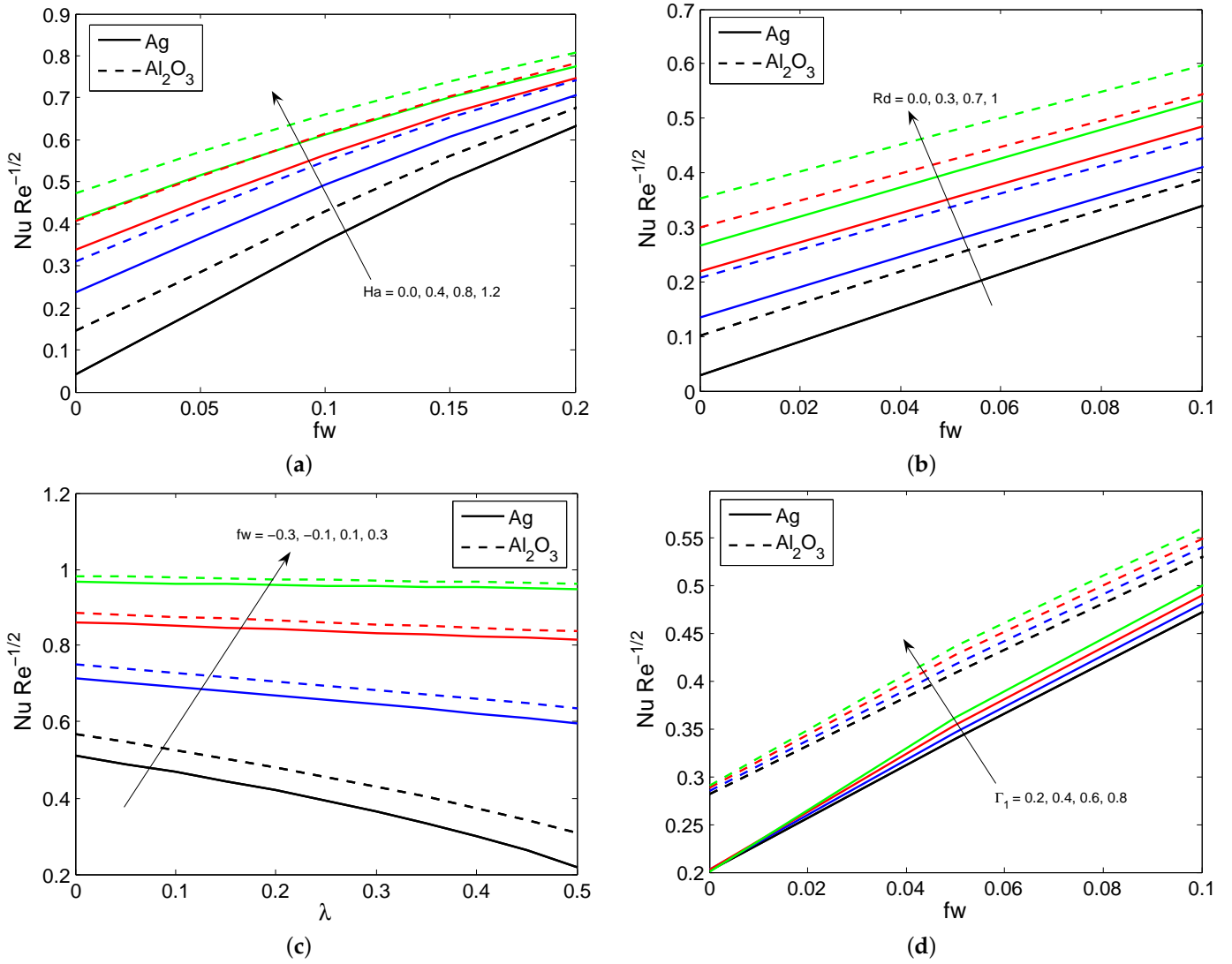


Figure 8. LNN variation for diverging values of (a)  $Ha$ , (b)  $Rd$ , (c)  $fw$  and (d)  $\Gamma_1$ .

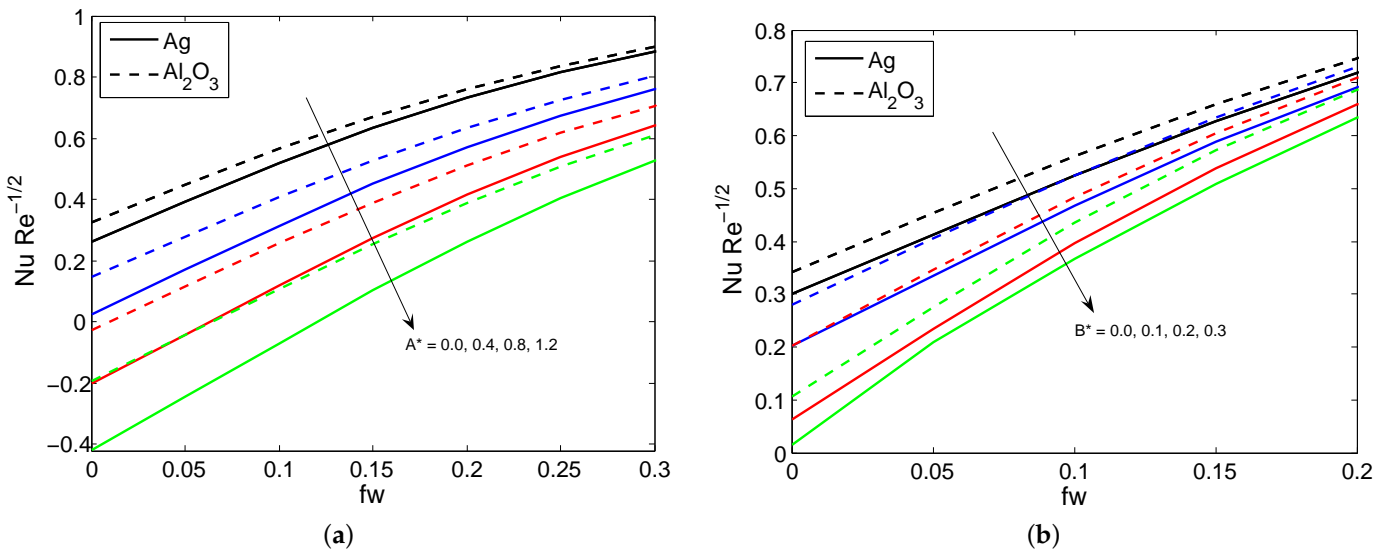


Figure 9. LNN variation for diverging values of (a)  $A^*$  and (b)  $B^*$ .

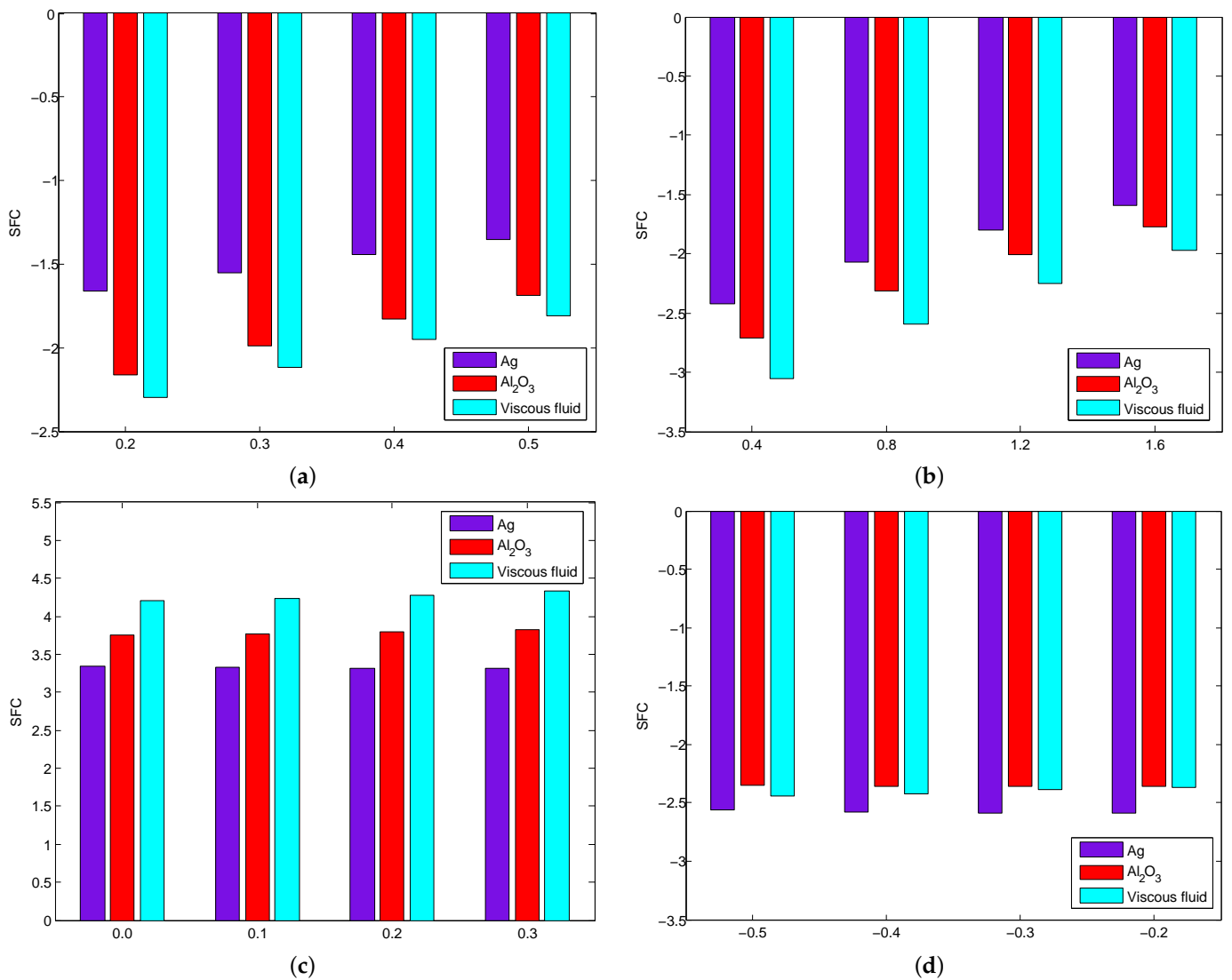


Figure 10. The increasing/declining percentage of SFC on (a)  $\lambda$ , (b)  $Fr$ , (c)  $Ha$  and (d)  $fw$ .

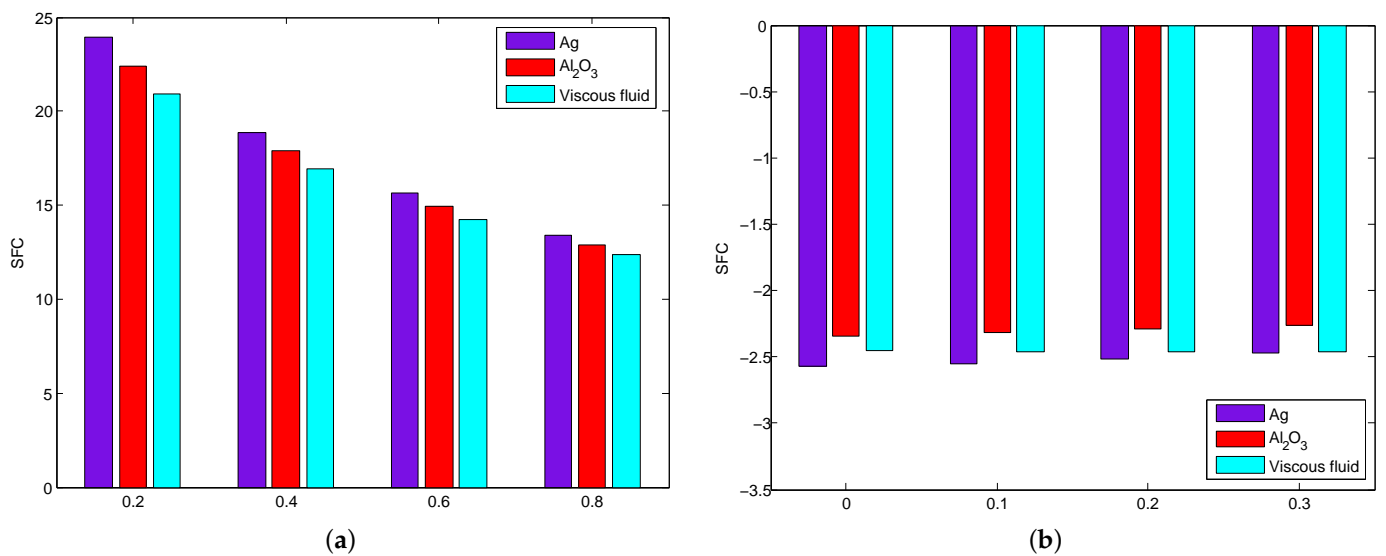


Figure 11. The increasing/declining percentage of SFC on (a)  $\Lambda$  and (b)  $fw$ .

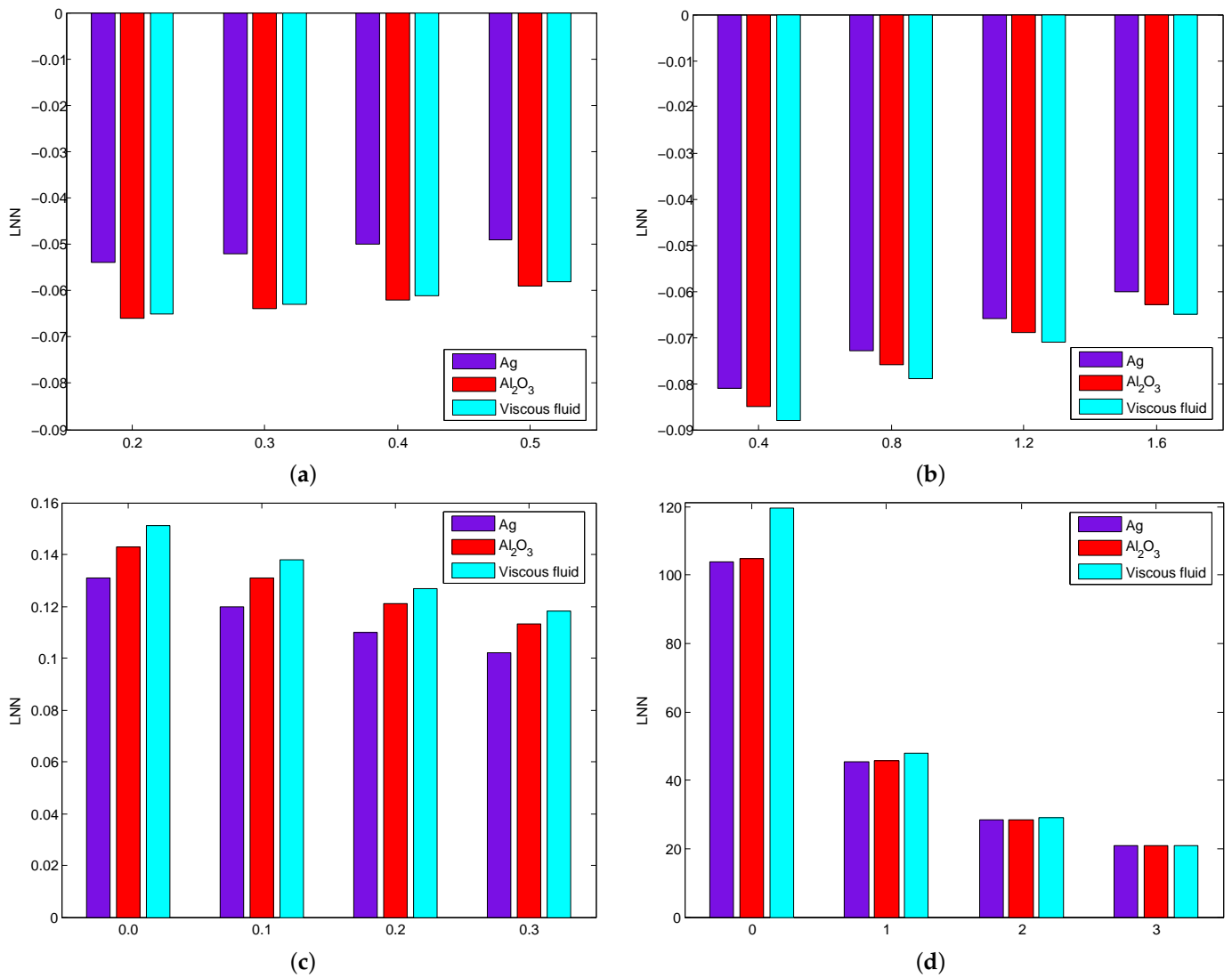


Figure 12. The increasing/declining percentage of LNN on (a)  $\lambda$ , (b)  $Fr$ , (c)  $Ha$  and (d)  $Rd$ .

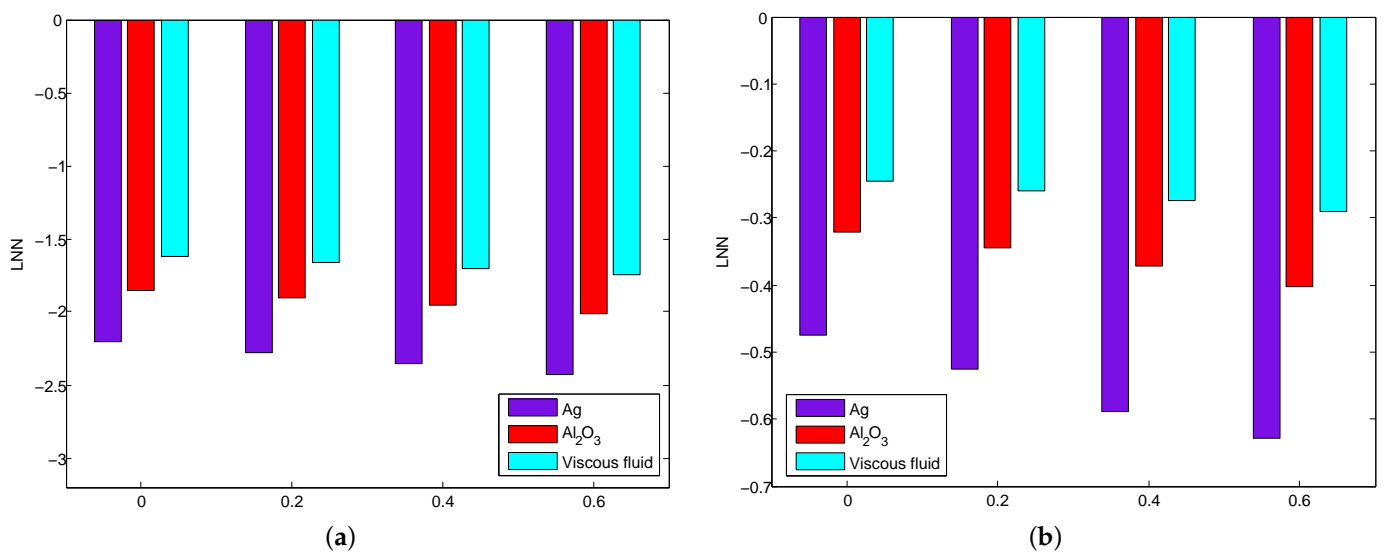
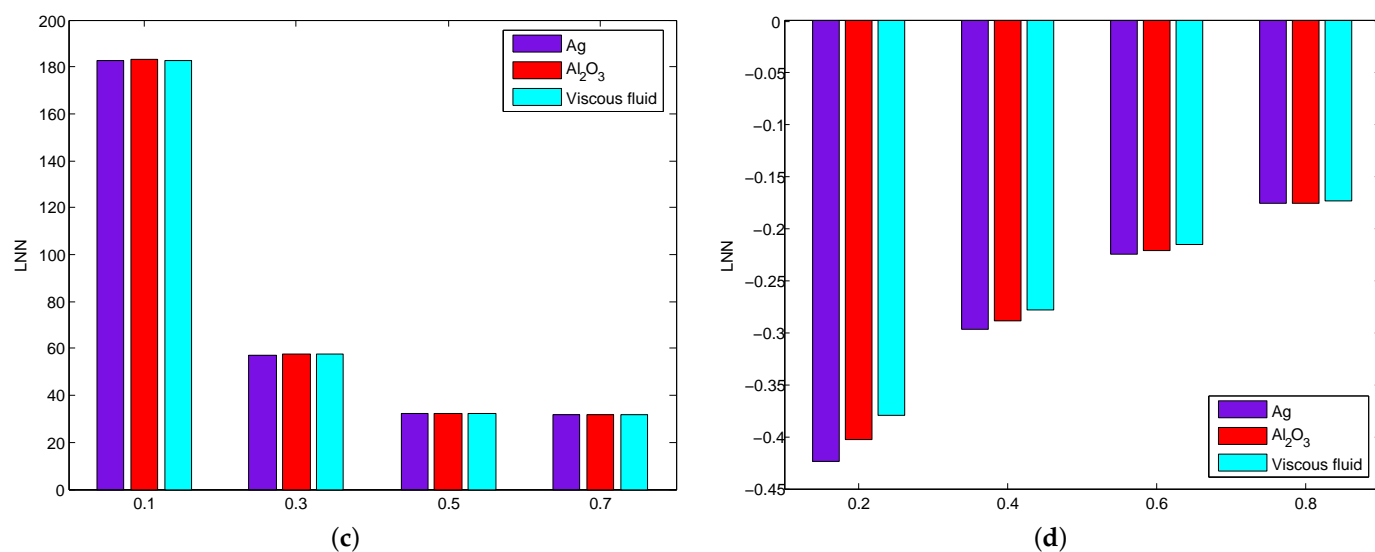


Figure 13. Cont.



**Figure 13.** The increasing/declining percentage of LNN on (a)  $A^*$ , (b)  $B^*$ , (c)  $Bi$  and (d)  $\Lambda$ .

## 5. Conclusions

The main purpose of this research is to scrutinize the consequences of Darcy–Forchheimer flow in water-based Ag/Al<sub>2</sub>O<sub>3</sub> nanofluid past a Riga plate. The energy equation is formed by including the Cattaneo–Christov heat flux, heat sink/source, and non-linear thermal radiation impacts. The governing models are re-framed by implementing suitable variables. The re-framed models are solved numerically by implementing the MATLAB bvp4c technique. The notable findings derived from the current study are as follows:

- The nanofluid velocity profile reduces for higher values of porosity, the Forchheimer number, the suction/injection parameter, and the slip parameter.
- The greater the thermal radiation, nanoparticle volume fraction, space and temperature dependent heat source parameter, the greater the nanofluid temperature profile.
- The nanofluid temperature declines for larger values of convection cooling, injection/suction and the thermal relaxation time parameter.
- The skin friction coefficient declines for increasing values of the Forchheimer number and suction/injection parameter, and increases when the modified Hartmann number increases.
- The heat transfer gradient increases with increasing values for the Hartmann number, radiation, suction/injection and the thermal relaxation time parameter, whereas it declines when the space and temperature dependent heat source parameter is increased.
- In future, we will expand this flow model by including hybrid and ternary hybrid nanofluids with different shape factors.

**Author Contributions:** Conceptualization, S.E. and K.L.; methodology, S.E.; software, K.L.; validation, S.E.; formal analysis, S.D.; investigation, K.L.; resources, S.D.; data curation, S.E.; writing—original draft preparation, S.D.; writing—review and editing, S.D. and S.E.; visualization, S.E.; supervision, S.E.; project administration, K.L.; funding acquisition, K.L. All authors have read and agreed to the published version of the manuscript.

**Funding:** This research received no external funding.

**Conflicts of Interest:** The authors declare no conflict of interest.

## Nomenclature

Symbols	Description
$a_1$	positive constants
$A^*$	space-dependent heat source parameter
$B^*$	temperature-dependent heat source parameter
$Bi \left( = \frac{h_c}{k_f} \sqrt{\frac{v_f}{a}} \right)$	Biot number
$C_p$	specific heat capacity
$c_b$	drag coefficient
$C_f$	skin friction coefficient
f	subscript represent base fluid
$f_w \left( = \frac{V_w}{\sqrt{a(v)_f}} \right)$	suction/injection parameter
$Fr \left( = \frac{c_b}{\sqrt{k_1^*}} \right)$	Forchheimer number
$h_c$	heat transfer coefficient
$Ha \left( = \frac{\pi J_0 M x}{8(\rho)_f a^2} \right)$	modified Hartmann number
$J_0$	current density applied to the electrodes
$k_1^*$	permeability of porous medium
$k^*$	Rosseland absorption coefficient
M	magnetic field
nf	subscript represent nanoliquid
$Nu$	Nusselt number
$Pr \left( = \frac{\alpha_f}{v_f} \right)$	Prandtl number
$Rd \left( = \frac{4\sigma^* T_\infty^3}{k^*(k)_f} \right)$	radiation parameter
$Re \left( = \frac{ax^2}{v_f} \right)$	local Reynolds number
T	fluid temperature
$T_f$	temperature of the hot fluid
$T_\infty$	ambient temperature
$u, v$	velocity components
$x, y$	Cartesian coordinates
$U_w, V_w$	surface stretching velocities
<b>Greek Symbols</b>	
$\rho$	density
$\mu$	dynamic viscosity
$\zeta$	dimensionless variable
$\theta$	dimensionless temperature
$\beta_R \left( = \frac{\pi}{a_1} \sqrt{\frac{v_f}{a}} \right)$	dimensionless parameter
$\theta_w \left( = \frac{T_f}{T_\infty} \right)$	heating variable
$\nu$	kinematic viscosity
$\lambda \left( = \frac{v_f}{k_1^* a} \right)$	local porosity parameter
$\phi$	nanoparticle volume fraction
$\psi$	stream function
$\sigma^*$	Stefen-Boltzmann constant
$\Lambda$	slip parameter
$\alpha$	thermal diffusivity
$\Gamma_1 \left( = \lambda a \right)$	thermal relaxation time parameter
<b>Abbreviations</b>	
LNN	local Nusselt number
MHD	magnetohydrodynamics
ODEs	ordinary differential equations
PDEs	partial differential equations
SFC	skin friction coefficient
SS	stretching sheet
TBL	thermal boundary layer

## References

1. Choi, S.U.; Eastman, J.A. *Enhancing Thermal Conductivity of Fluids with Nanoparticles*. (No. ANL/MSD/CP-84938; CONF-951135-29); Argonne National Lab. (ANL): Argonne, IL, USA, 1995.
2. Martin, E.; Sastre, F.; Velazquez, A.; Bairi, A. Heat transfer enhancement around a finned vertical antenna by means of porous media saturated with Water-Copper nanofluid. *Case Stud. Therm. Eng.* **2021**, *28*, 101555. [[CrossRef](#)]
3. Uddin, M.J.; Al-Balushi, J.; Mahatabuddin, S.; Rahman, M.M. Convective heat transport for copper oxide-water nanofluid in an isosceles triangular cavity with a rippled base wall in the presence of magnetic field. *Int. J. Thermofluid* **2022**, *16*, 100195. [[CrossRef](#)]
4. Nayak, M.K.; Shaw, S.; Khan, M.I.; Pandey, V.S.; Nazeer, M. Flow and thermal analysis on Darcy–Forchheimer flow of copper-water nanofluid due to a rotating disk: A static and dynamic approach. *J. Mater. Res. Technol.* **2020**, *9*, 7387–7408. [[CrossRef](#)]
5. Adem, G.A.; Kishan, N. Slip effects in a flow and heat transfer of a nanofluid over a nonlinearly stretching sheet using optimal homotopy asymptotic method. *Int. J. Eng. Manuf. Sci.* **2018**, *8*, 25–46.
6. Uddin, M.J.; Rasel, S.K.; Adewole, J.K.; Al Kalbani, K.S. Finite element simulation on the convective double diffusive water-based copper oxide nanofluid flow in a square cavity having vertical wavy surfaces in presence of hydro-magnetic field. *Results Eng.* **2022**, *13*, 100364. [[CrossRef](#)]
7. Verma, A.K.; Rajput, S.; Bhattacharyya, K.; Chamkha, A.J. Nanoparticle’s radius effect on unsteady mixed convective copper-water nanofluid flow over an expanding sheet in porous medium with boundary slip. *J. Adv. Chem. Eng.* **2022**, *12*, 100366. [[CrossRef](#)]
8. Yousef, N.S.; Megahed, A.M.; Ghoneim, N.I.; Elsafi, M.; Fares, E. Chemical reaction impact on MHD dissipative Casson-Williamson nanofluid flow over a slippery stretching sheet through porous medium. *Alex. Eng. J.* **2022**, *61*, 10161–10170. [[CrossRef](#)]
9. Mohamed, M.K.A.; Ong, H.R.; Alkasasbeh, H.T.; Salleh, M.Z. Heat Transfer of Ag – Al<sub>2</sub>O<sub>3</sub>/Water Hybrid Nanofluid on a Stagnation Point Flow over a Stretching Sheet with Newtonian Heating. *J. Phys. Conf. Ser.* **2020**, *1529*, 042085. [[CrossRef](#)]
10. Shahzad, A.; Liaqat, F.; Ellahi, Z.; Sohail, M.; Ayub, M.; Ali, M.R. Thin film flow and heat transfer of Cu-nanofluids with slip and convective boundary condition over a stretching sheet. *Sci. Rep.* **2022**, *12*, 14254. [[CrossRef](#)]
11. Gailitis, A.; Lielausis, O. On a possibility to reduce the hydrodynamic resistance of a plate in an electrolyte. *Appl. Magneto hydrodyn.* **1961**, *12*, 143–146.
12. Vaidya, H.; Prasad, K.V.; Tlili, I.; Makinde, O.D.; Rajashekhar, C.; Khan, S.U.; Kumar, R.; Mahendra, D.L. Mixed convective nanofluid flow over a non linearly stretched Riga plate. *Case Stud. Therm. Eng.* **2021**, *24*, 100828. [[CrossRef](#)]
13. Shah, S.; Hussain, S.; Sagheer, M. Impacts of variable thermal conductivity on stagnation point boundary layer flow past a Riga plate with variable thickness using generalized Fourier’s law. *Results Phys.* **2018**, *9*, 303–312. [[CrossRef](#)]
14. Rizwana, R.; Nadeem, S. Series solution of unsteady MHD oblique stagnation point flow of copper-water nanofluid flow towards Riga plate. *Heliyon* **2020**, *6*, e04689. [[CrossRef](#)]
15. Ramesh, G.K.; Roopa, G.S.; Gireesha, B.J.; Shehzad, S.A.; Abbasi, F.M. An electro-magneto-hydrodynamic flow Maxwell nanoliquid past a Riga plate: A numerical study. *J. Braz. Soc. Mech. Sci. Eng.* **2017**, *39*, 4547–4554. [[CrossRef](#)]
16. Abbas, T.; Ayub, M.; Bhatti, M.M.; Rashidi, M.M.; Ali, M.E.S. Entropy generation on nanofluid flow through a horizontal Riga plate. *Entropy* **2016**, *18*, 223. [[CrossRef](#)]
17. Waqas, H.; Kafait, A.; Muhammad, T.; Farooq, U. Numerical study for bio-convection flow of tangent hyperbolic nanofluid over a Riga plate with activation energy. *Alex. Eng. J.* **2022**, *61*, 1803–1814. [[CrossRef](#)]
18. Eswaramoorthi, S.; Alessa, N.; Sangeethavaanee, M.; Namgyel, N. Numerical and Analytical Investigation for Darcy–Forchheimer Flow of a Williamson Fluid over a Riga Plate with Double Stratification and Cattaneo–Christov Dual Flux. *Adv. Math. Phys.* **2021**, *2021*, 1867824. [[CrossRef](#)]
19. Faizan, M.; Ali, F.; Loganathan, K.; Zaib, A.; Reddy, C.A.; Abdelsalam, S.I. Entropy Analysis of Sutterby Nanofluid Flow over a Riga Sheet with Gyrotactic Microorganisms and Cattaneo–Christov Double Diffusion. *Mathematics* **2022**, *10*, 3157. [[CrossRef](#)]
20. Karthik, T.S.; Loganathan, K.; Shankar, A.N.; Carmichael, M.J.; Mohan, A.; Kaabar, M.K.; Kayikci, S. Zero and nonzero mass flux effects of bioconvective viscoelastic nanofluid over a 3D Riga surface with the swimming of gyrotactic microorganisms. *Adv. Math. Phys.* **2021**, *2021*, 9914134. [[CrossRef](#)]
21. Parvine, M.; Alam, M.M. Nano fluid flow along the Riga plate with electromagnetic field in a rotating system. *AIP Conf. Proc.* **2019**, *2121*, 070003.
22. Rafique, K.; Alotaibi, H.; Ibrar, N.; Khan, I. Stratified Flow of Micropolar Nanofluid over Riga Plate: Numerical Analysis. *Energies* **2022**, *15*, 316.
23. Madhukesh, J.K.; Ramesh, G.K.; Aly, E.H.; Chamkha, A.J. Dynamics of water conveying SWCNT nanoparticles and swimming microorganisms over a Riga plate subject to heat source/sink. *Alex. Eng. J.* **2022**, *61*, 2418–2429. [[CrossRef](#)]
24. Oke, A.S.; Animasaun, I.L.; Mutuku, W.N.; Kimathi, M.; Shah, N.A.; Saleem, S. Significance of Coriolis force, volume fraction, and heat source/sink on the dynamics of water conveying 47 nm alumina nanoparticles over a uniform surface. *Chin. J. Phys.* **2021**, *71*, 716–727. [[CrossRef](#)]
25. Qasim, M. Heat and mass transfer in a Jeffrey fluid over a stretching sheet with heat source/sink. *Alex. Eng. J.* **2013**, *52*, 571–575. [[CrossRef](#)]

26. Sharma, B.K.; Gandhi, R. Combined effects of Joule heating and non-uniform heat source/sink on unsteady MHD mixed convective flow over a vertical stretching surface embedded in a Darcy–Forchheimer porous medium. *Propuls. Power Res.* **2022**, *11*, 276–292. [[CrossRef](#)]
27. Vieru, D.; Fetecau, C.; Shah, N.A.; Yook, S.J. Unsteady natural convection flow due to fractional thermal transport and symmetric heat source/sink. *Alex. Eng. J.* **2022**, *64*, 761–770. [[CrossRef](#)]
28. Sandeep, N.; Sulochana, C. Momentum and heat transfer behaviour of Jeffrey, Maxwell and Oldroyd-B nanofluids past a stretching surface with non-uniform heat source/sink. *Ain Shams Eng. J.* **2018**, *9*, 517–524. [[CrossRef](#)]
29. Jena, S.; Dash, G.C.; Mishra, S.R. Chemical reaction effect on MHD viscoelastic fluid flow over a vertical stretching sheet with heat source/sink. *Ain Shams Eng. J.* **2018**, *9*, 1205–1213. [[CrossRef](#)]
30. Sandeep, N.; Sulochana, C. Dual solutions for unsteady mixed convection flow of MHD micropolar fluid over a stretching/shrinking sheet with non-uniform heat source/sink. *Eng. Sci. Technol. Int. J.* **2015**, *18*, 738–745. [[CrossRef](#)]
31. Reddy, P.S.; Rao, K.S. MHD natural convection heat and mass transfer of Al<sub>2</sub>O<sub>3</sub>-water and Ag-water nanofluids over a vertical cone with chemical reaction. *Procedia Eng.* **2015**, *127*, 476–484. [[CrossRef](#)]
32. Khan, U.; Zaib, A.; Ishak, A.; Alotaibi, A.M.; Eldin, S.M.; Akkurt, N.; Waini, I.; Madhukesh, J.K. Stability Analysis of Buoyancy Magneto Flow of Hybrid Nanofluid through a Stretchable/Shrinkable Vertical Sheet Induced by a Micropolar Fluid Subject to Nonlinear Heat Sink/Source. *Magnetochemistry* **2022**, *8*, 188. [[CrossRef](#)]
33. Yu, Y.; Khan, U.; Zaib, A.; Ishak, A.; Waini, I.; Raizah, Z.; Galal, A.M. Exploration of 3D stagnation-point flow induced by nanofluid through a horizontal plane surface saturated in a porous medium with generalized slip effects. *Ain Shams Eng. J.* **2023**, *14*, 101873. [[CrossRef](#)]
34. Rashidi, M.M.; Ganesh, N.V.; Hakeem, A.A.; Ganga, B. Buoyancy effect on MHD flow of nanofluid over a stretching sheet in the presence of thermal radiation. *J. Mol. Liq.* **2014**, *198*, 234–238. [[CrossRef](#)]
35. Kameswaran, P.K.; Sibanda, P.; Murti, A.S.N. Nanofluid flow over a permeable surface with convective boundary conditions and radiative heat transfer. *Math. Probl. Eng.* **2013**, *2013*, 201219. [[CrossRef](#)]
36. Maleki, H.; Alsarraf, J.; Moghanizadeh, A.; Hajabdollahi, H.; Safaei, M.R. Heat transfer and nanofluid flow over a porous plate with radiation and slip boundary conditions. *J. Cent. South Univ.* **2019**, *26*, 1099–1115. [[CrossRef](#)]
37. Eswaramoorthi, S.; Loganathan, K.; Jain, R.; Gyeltshen, S. Darcy–Forchheimer 3D Flow of Glycerin-Based Carbon Nanotubes on a Riga Plate with Nonlinear Thermal Radiation and Cattaneo–Christov Heat Flux. *J. Nanomater.* **2022**, *2022*, 5286921. [[CrossRef](#)]
38. Mahat, R.; Saqib, M.; Khan, I.; Shafie, S.; Noor, N.A.M. Thermal radiation effect on Viscoelastic Walters’-B nanofluid flow through a circular cylinder in convective and constant heat flux. *Case Stud. Therm. Eng.* **2022**, *39*, 102394. [[CrossRef](#)]
39. Mahanthesh, B.; Giresha, B.J.; Animasaun, I.L. Exploration of non-linear thermal radiation and suspended nanoparticles effects on mixed convection boundary layer flow of nanoliquids on a melting vertical surface. *J. Nanofluids* **2018**, *7*, 833–843. [[CrossRef](#)]
40. Bhatti, M.M.; Al-Khaled, K.; Khan, S.U.; Chamam, W.; Awais, M. Darcy–Forchheimer higher-order slip flow of Eyring–Powell nanofluid with nonlinear thermal radiation and bioconvection phenomenon. *J. Dispers. Sci. Technol.* **2021**, 1–11. [[CrossRef](#)]
41. Eswaramoorthi, S.; Thamaraiselvi, S.; Loganathan, K. Exploration of Darcy–Forchheimer Flows of Non-Newtonian Casson and Williamson Conveying Tiny Particles Experiencing Binary Chemical Reaction and Thermal Radiation: Comparative Analysis. *Math. Comput. Appl.* **2022**, *27*, 52. [[CrossRef](#)]
42. Mahanta, G.; Das, M.; Nayak, M.K.; Shaw, S. Irreversibility analysis of 3D magnetohydrodynamic Casson nanofluid flow past through two bi-directional stretching surfaces with nonlinear radiation. *J. Nanofluids* **2021**, *10*, 316–326. [[CrossRef](#)]
43. Waqas, M.; Khan, U.; Zaib, A.; Ishak, A.; Albaqami, M.D.; Waini, I.; Alotabi, R.G.; Pop, I. Radiation effect on MHD three-dimensional stagnation-point flow comprising water-based graphene oxide nanofluid induced by a nonuniform heat source/sink over a horizontal plane surface. *Int. J. Mod. Phys. B* **2022**, *2022*, 2350146. [[CrossRef](#)]
44. Jha, B.K.; Samaila, G. The role of thermal radiation on the boundary layer past a stationary flat plate with constant surface boundary condition. *J. Nat.* **2022**, *2*, 7–11. [[CrossRef](#)]
45. Eswaramoorthi, S.; Divya, S.; Faisal, M.; Namgyel, N. Entropy and heat transfer analysis for MHD flow of-water-based nanofluid on a heated 3D plate with nonlinear radiation. *Math. Probl. Eng.* **2022**, *2022*, 7319988.
46. Alzahrani, H.A.; Alsaiari, A.; Madhukesh, J.K.; Naveen Kumar, R.; Prasanna, B.M. Effect of thermal radiation on heat transfer in plane wall jet flow of Casson nanofluid with suction subject to a slip boundary condition. *Waves Random Complex Media* **2022**, 1–18. [[CrossRef](#)]
47. Aldabesh, A.; Khan, S.U.; Habib, D.; Waqas, H.; Tlili, I.; Khan, M.I.; Khan, W.A. Unsteady transient slip flow of Williamson nanofluid containing gyrotactic microorganism and activation energy. *Alex. Eng. J.* **2020**, *59*, 4315–4328. [[CrossRef](#)]
48. Mahmood, A.; Jamshed, W.; Aziz, A. Entropy and heat transfer analysis using Cattaneo–Christov heat flux model for a boundary layer flow of Casson nanoliquid. *Results Phys.* **2018**, *10*, 640–649. [[CrossRef](#)]
49. Hayat, T.; Khan, M.I.; Khan, T.A.; Khan, M.I.; Ahmad, S.; Alsaedi, A. Entropy generation in Darcy–Forchheimer bidirectional flow of water-based carbon nanotubes with convective boundary condition. *J. Mol. Liq.* **2018**, *265*, 629–638. [[CrossRef](#)]
50. Afify, A.A. The influence of slip boundary condition on Casson nanofluid flow over a stretching sheet in the presence of viscous dissipation and chemical reaction. *Math. Probl. Eng.* **2017**, *2017*, 3804751. [[CrossRef](#)]

51. Asshaari, I.; Jedi, A.; Abdullah, S. Brownian Motion and Thermophoresis Effects in co-Flowing Carbon Nanotubes towards a Moving Plate. *Results Phys.* **2022**, *44*, 106165. [[CrossRef](#)]
52. Shampine, L.F.; Kierzenka, J.; Reichelt, M.W. Solving boundary value problems for ordinary differential equations in MATLAB with bvp4c. *World J. Mech.* **2013**, *3*, 1–27.
53. Shampine, L.F.; Gladwell, I.; Thompson, I. *Solving ODEs with MATLAB*, 1st ed.; Cambridge University Press: Cambridge, UK, 2003.
54. Prabakaran, R.; Eswaramoorthi, S.; Loganathan, K.; Gyeltshen, S. Thermal Radiation and Viscous Dissipation Impacts of Water and Kerosene-Based Carbon Nanotubes over a Heated Riga Sheet. *J. Nanomater.* **2022**, *2022*, 1865763.
55. Ibrahim, W.; Shankar, B. MHD boundary layer flow and heat transfer of a nanofluid past a permeable stretching sheet with velocity, thermal and solutal slip boundary conditions. *Comput. Fluids* **2013**, *75*, 1–10.
56. Roja, A.; Gireesha, B.J. Impact of Hall and Ion effects on MHD couple stress nanofluid flow through an inclined channel subjected to convective, hydraulic slip, heat generation, and thermal radiation. *Heat Transf.* **2020**, *49*, 3314–3333.

**Disclaimer/Publisher’s Note:** The statements, opinions and data contained in all publications are solely those of the individual author(s) and contributor(s) and not of MDPI and/or the editor(s). MDPI and/or the editor(s) disclaim responsibility for any injury to people or property resulting from any ideas, methods, instructions or products referred to in the content.